3-5 points provide readers with the main findings of the article

Each highlight is 85 characters or less

No acronyms or abbreviations

Highlights:

- Cold-rolling leads to increased amounts of grain boundaries and dislocations.
- Cold-rolling increases the susceptibly of 316L alloy to corrosion in molten salt.
- Grain boundaries and dislocations govern corrosion resistance.
- Alloying elements diffuse to grain boundaries and dislocations.
- Alloying elements react with molten salt to form Cr, Mo corrosion products.

The Effect of Cold-Rolling on the Microstructure and Corrosion Behaviour of 316L Alloy in FLiNaK Molten Salt

M. Maric[1,2], O. Muránsky[1,2*], I. Karatchevtseva[1], T. Ungár[3],
J. Hester[1], A. Studer[1], N. Scales[1], G. Ribárik[3], S. Primig[2], M.R. Hill[4]

[1] Australian Science and Technology Organization (ANSTO), Sydney, NSW, Australia
[2] School of Materials Science and Engineering, UNSW Sydney, Sydney, Australia
[3] Eötvös Loránd University, Department of Materials Physics, Budapest, Hungary
[4] University of California, Mechanical and Aeronautical Engineering Department, Davis, USA

Abstract

The effect of cold-rolling on the microstructure and molten salt corrosion behaviour of 316L alloy was investigated. Corrosion tests were performed in FLiNaK salt at 600 °C for 300h. The present results indicate that cold-rolling leads to enhanced corrosion in molten salt despite its beneficial effect on the alloys mechanical properties. It is shown that the corrosion resistance of cold-rolled 316L alloy is largely governed by the presence of high-angle grain boundaries (HAGBs) and geometrically-necessary dislocations (GNDs). Exacerbated corrosion is thus directly related to the increased prevalence of grain boundaries and dislocations within the microstructure.

Keywords: 316L; cold-rolling; molten salt corrosion; microstructure; dislocation density

Corresponding authors: E-mail: ondrej.muransky@ansto.gov.au, Tel.: +61 (0)2 9717 3488

1. Introduction

Molten Salt Reactors (MSRs) are one of the Generation IV reactor systems currently under development. MSR systems are designed to use either liquid fuel (fuel is dissolved in molten salt – Molten Salt Fast Reactors, MSFRs), or solid fuel (molten salt is used only as a coolant while fuel is solid - Advanced High Temperature Reactors, AHTRs) [1, 2]. The most significant advantage of molten salt is that it remains in the liquid state over a very wide range of temperatures at atmospheric pressure - thus inherently preventing an explosion-like accident of the system. Additionally, molten salt has advantageous thermo-physical properties such as high thermal diffusivity, relatively low viscosity, and it is both non-flammable and inert [1-3]. Owing to these advantageous thermo-physical properties, extensive research into applications of molten salts within the nuclear industry has occurred since the development of the first MSR at the Oak Ridge National Laboratory in the 1950 - 1970s [1]. Furthermore, molten salt is also being considered as a heat-transfer and heat-storage medium in Concentrated Solar Thermal (CST) plants and Thermal Energy Storage (TES) applications [4]. Hence, the identification and assessment of degradation mechanisms of materials in molten salt environments is of high technological importance for the rapid development and deployment of these molten-salt based future energy generation and storage systems.

The main driving force for materials degradation in molten salt environments is corrosion, which is driven by the thermodynamic tendency of the alloying elements (Ni, Mo, Cr, Fe) present within most structural alloys to form compounds with the constituents of the molten salt (e.g. fluorides in FLiNaK, FLiBe molten salts). Studies conducted by Olson et al. in FLiNaK molten salt [5] highlighted that the fluoridation of Cr and Fe is highly likely due to their favourable Redox potential – i.e. negative Gibbs free energy of formation of fluorine based corrosion products. In addition, accelerated corrosion can occur due to the presence of commonly found impurities in fluoride molten salts (SO_4^{2-}, Cl^-, H_2O) [6-8]. It is thus important to closely control the purity of the salt during the operation of any molten-salt based system. Employed structural materials need to possess not only good molten-salt corrosion resistance, but also high-temperature creep resistance, high-temperature stability, and, in the case of MSRs, sound resistance to radiation damage (radiation-induced swelling, embrittlement, hardening, and creep), whilst still being safe and economically viable [9-12].

316L stainless steel is already extensively utilised within the nuclear industry and is also being considered as the structural material for applications in future MSR systems [13], as well as in combined CST - TES energy-generation and energy-storage systems. In most aerated environments, the 316L alloy has superior corrosion resistance due to its high Cr and low C content. The high level of Cr enables the formation of a uniform well-dispersed passive Cr_2O_3 film while the low C content inhibits the precipitation of Cr into Cr carbides (sensitization), which would decrease the corrosion resistance of the alloy [14-16]. However, studies measuring the corrosion resistance of 316L alloy in fluoride molten salt environments have shown that corrosion is a prevalent mechanism of failure [13]. This is because, in these

environments, the protective chromium film becomes unstable and increasingly prone to dissolution (producing CrF_3 and CrF_4) [13, 16, 17].

In attempts to improve the mechanical properties of the 316L alloy, various mechanical treatments such as cold-rolling, laser peening and sandblasting are typically utilized. These treatments are cheaper alternatives to the development of new alloys, which would also require lengthy and costly standardisation processes [12, 18]. Cold rolling is a simple and cost effective process that is performed on ductile materials in order to improve their mechanical properties [19]. However, recent studies have shown that increasing the extent of cold rolling worsens the corrosion resistance and makes the material more susceptible to stress corrosion cracking (SCC) in Light Water Reactors [20, 21]. It is thus important to understand the mechanisms and microstructural factors that influence the corrosion resistance of cold-rolled alloys in general.

The present study investigates the effect of cold rolling on the microstructure and molten-salt corrosion of the AISI 316L alloy in LiF (46.5 mol.%) – NaF (11.5 mol.%) – KF (42 mol.%) eutectic salt mixture (FLiNaK) at 600 °C after 300 h of exposure. The 316L alloy was subjected to 0%, 20% and 30% reductions in thickness by the cold rolling process before undergoing corrosion testing in FLiNaK molten salt. It is shown that with increased amounts of cold-rolling, the corrosion resistance of the alloy decreases as shown by the increasing mass loss of material during exposure to the molten salt. The decreasing corrosion resistance of the cold-rolled material is related to the increased prevalence of low- and high- angle grain boundaries as well as crystallographic defects particularly dislocations. The aim of this study is to reveal the interplay between these microstructural characteristics and molten-salt corrosion by using an array of microscopic (Scanning Electron Microscopy (SEM), Electron Backscatter Diffraction (EBSD), Energy Dispersive X-Ray Spectroscopy (EDS), Electron Micro Probe Analyzer (EPMA) and diffraction (high resolution neutron diffraction) techniques.

2. Experimental

2.1 Material

Three AISI 316L (ASME SA240, Table 1) stainless steel plates (610344-3A) with dimensions of 127 (x) × 25.4 (y) × 355.6 (z) mm^3 (Fig. 1) were sourced from the American Stainless Steel Corp. The plates were hot-rolled, solution-annealed, water-cooled, and pickled in accordance with the ASME SA-240 standards before being unidirectionally cold-rolled in order to attain 20% and 30% reductions in plate thickness. One plate was kept in the as-received condition for direct comparison (0% cold-rolled).

The post-cold-rolled plate thickness (y) and mechanical properties yield strength (YS), ultimate tensile strength (UTS), total elongation (TE) and Rockwell hardness (RWH) of studied plates (0%, 20%, and 30%) are summarised in Table 2. The mechanical testing was done at the University of California Davis in both TD (x) and RD (z) directions. Two measurements from both the TD and RD were then averaged and are reported in Table 2.

Owing to the high Cr and relatively low Ni content, the microstructure consists of γ-matrix (fcc) and δ-ferrite (bcc). The volume fraction of δ-ferrite in the studied alloy was found to be approximately 5 wt.%. This was determined empirically from the Schaeffler diagram and experimentally by Rietveld (GSAS-II [22]) refinement of the high-resolution neutron diffraction (HRND) patterns. These were collected using the HRND instrument ECHIDNA at Australian Nuclear Science and Technology Organisation (ANSTO) (see Appendix 1).

The crystallographic texture of γ-austenite phase (fcc) of 0%, 20%, and 30% cold-rolled conditions was measured using the high-intensity neutron diffraction (HIND) instrument WOMBAT at ANSTO. Texture analysis was done using the MTEX toolbox [23] and final pole figure plotting using the pod2k software [24]. Fig. 2 presents a comparison of the (111) pole figures of the three different samples – these measurements affirm the typical rolling texture of materials with fcc crystal lattice structure and show that there is a sharp increase in the crystallographic texture as a consequence of cold rolling. Interestingly, the texture is roughly the same for 20% and 30% cold-rolled conditions. The crystallographic texture of the δ-ferrite phase (bcc) has not been studied.

Electric discharge machining was used to extract samples for electron microscopy, neutron diffraction and molten salt testing. As schematically shown in Fig. 1 each plate was first cut to half of the thickness of the plate (y/2) before being sectioned into small test samples. It was thus assumed that the microstructure is symmetric about the plate half thickness plane (y/2). All the samples are cut perpendicular to rolling direction (RD) as shown in Fig. 1 – the microstructural observations are made on TD-ND (x-y) plane. Hence, the present study does not consider the effect of crystallographic texture or grain morphology in different directions on the corrosion performance of the alloy. The samples for microscopic and corrosion testing were polished in three stages: i) fine grinding, ii) diamond polishing and iii) oxide polishing, each stage was repeated three times at varying abrasive particle sizes and applied forces. Note, that samples were also polished prior to corrosion testing.

2.2 Electron microscopy

The pre- and post- corrosion microstructure was characterised using a Zeiss Ultra Plus SEM equipped with an Oxford Instruments HKL NordlysS EBSD and EDS detectors. The following parameters were kept constant during the acquisition of EBSD orientation maps: a step size of 0.14 µm, accelerating voltage of 20keV and a tilt angle of 70°, while the working distance was kept between 14.5 and 15 mm. The EBSD orientation maps were then analysed using and the Matlab MTEX toolbox [25]. In the first step the raw EBSD data was filtered such that any data points with mean angular deviation (MAD) greater than 0.8° and band contrast below 0.1 were excluded from further data analyses. In the second step, the mean average filter of 7×7 was used to reduce the noise in experimental data. Finally, the typical microstructural characteristics were calculated. In order to obtain bulk characteristics of studied alloy conditions numerous EBSD orientation maps at different locations across the sample thickness were collected and obtained results were averaged (see below).

2.3 Neutron diffraction

The high-resolution neutron diffractometer (HRND) ECHIDNA at the ANSTO OPAL research reactor was utilized for the measurement of dislocation density via peak broadening analysis of HRND patterns. ECHINDA was employed to obtain HRND patterns with high counting statistic necessary for the peak-broadening analysis of diffraction patterns. The HRND patterns were continuously collected for 12 hours, while the sample was fully submerged in the neutron beam and rotated around its y axis (see Fig. 1). The HRND patterns were then analysed using the Convolutional Multiple Whole Profile (CMWP) software packages [26-28] (see Appendix 1).

In CMWP [26-28] the *strain peak-broadening function* is defined directly by total dislocation density (ρ_T), the dislocation contrast factors (C), and the dislocation arrangement parameter (M), while the *particle size peak-broadening* is defined by median (m), and the variance (σ) of size distribution of coherently scattering domains (CSDs). Lastly, the *planar defects peak-broadening function* is defined as the sum of symmetric and antisymmetric Lorentz functions versus the density of the planar faults [29, 30]. The calculated diffraction patterns are produced by convoluting the defect-related, theoretically calculated peak-broadening functions and instrumental peak-broadening function. CMWP uses a combination of Levenberg–Marquardt least-squares and a Monte-Carlo statistical procedure [28] to find the best match between measured and modelled diffraction patterns. The two procedures are applied iteratively in order to obtain the global minimum for the above-mentioned physical parameters. The instrumental resolution (i.e. instrumental peak-broadening) of the ECHIDNA instrument, which is required as an input for CMWP analysis was determined by measurement of the LaB_6 powder standard.

2.4 Corrosion Testing

The corrosion tests were performed at ANSTO in a dedicated in-house developed molten salt rig wherein the samples were fully immersed in the LiF(46.5 mol.%) - NaF(11.5 mol.%) - KF(42 mol.%) eutectic mixture (FLiNaK) at 600 °C for 300h. 200 g of the FLiNaK salt was prepared in a glow box under a nitrogen atmosphere from commercially available LiF (62497), NaF (201154) and KF (60239) salts supplied by Sigma-Aldrich (≥ 99.0% pure). The maximum amounts of impurities in the produced FLiNaK salt were calculated based on the supplier datasheets and are shown in Appendix 2. No additional purification of the salt was applied in order to test the alloy in the molten salt containing commonly present impurities in particular SO_4^{2-}, Cl^-, and O^{2-}, which are known to accelerate corrosion. A vitreous (glassy) carbon crucible (7 mm in diameter, 7 mm in height and with the volume capacity of 250 ml) was filled with 200 g of prepared FLiNaK molten salt mixture in the glove box under a nitrogen atmosphere. The crucible was then placed in a pre-heated furnace (150 °C) and heated incrementally to 600 °C at a rate of 2-3 °C/min under vacuum until a pressure of 0.5 - 0.6 mbars was attained. This process is referred to as salt bake-out process (about 48 h long process) and is intended to minimize the amount of H_2O in the system. Once this pressure was reached, the furnace was purged with Ar gas (99.997%) at a pressure of 34 kPa. After the bake-out process, a salt sample was taken, and

analysed by Inductively Coupled Plasma Mass Spectrometry (ICP-MS) for the presence of metal ions (Cr, Fe, Mn, Ni, and Mo). Then, the samples (12 in total, 4 of each condition - 0%, 20% and 30%) were introduced into the molten salt so that they were fully submerged, whilst not being in direct contact with any side of the crucible. The temperature during the corrosion test was controlled with a thermocouple placed alongside the samples into the molten salt.

The samples were weighed with a high-precision scale both before and after the corrosion tests in order to record the material mass loss (per sample surface area) during the corrosion test. Four different samples at each level of cold rolling (0%, 20% and 30%) were tested at the same time to obtain average mass loss values and confirm the repeatability of the obtained results. The depth of corrosion attack was determined by measuring the corrosion penetration from the SEM images. Up to 100 depth measurements were taken on each sample, and an average value was calculated. In addition, the ICP-MS elemental analysis was performed after the testing to identify elements present in the salt (leaking out of the tested alloy) and check whether the equilibrium in any element concertation was reached.

3. Results and discussion

3.1 Effect of cold-rolling on microstructure

EBSD and HRND techniques were employed in order to investigate the impact of cold-rolling on the microstructure of the 316L alloy. These techniques provide complimentary information about the microstructure, however, unlike HRND, EBSD does not provide microstructure-average (bulk) information. Hence, a number of EBSD orientation maps (up to 10) at different locations across the microstructure were collected and the results were then averaged in order to obtain microstructure-average (bulk) information (characteristics) of the microstructure.

Fig. 3 shows EBSD maps (microstructure) of the studied 316L alloy in annealed (Fig. 3a,d) and cold-rolled (Fig. 3b,c,e,f) conditions. Their direct comparison clearly shows the impact of cold-rolling on the microstructure of the alloy. It becomes clear that with an increasing amount of cold-rolling, the length of grain boundaries increases significantly (Fig.3d,e,f). In the framework of this study, general high-angle grain boundaries (HAGBs) are defined as any boundary with a misorientation angle greater than 5 degrees (shown in black), twin boundaries are classified as specific types of HAGBs with a misorientation angle of 60° degrees (shown in red), and grain boundaries between δ-ferrite and γ-austenite are shown in green. As shown in Fig. 3, there are no deformation twins present in the annealed sample, whilst there are significant amount of deformation twins present in both the 20% and 30% cold-rolled samples. Note, that any twins present in the annealed (0%) specimen, should be referred to as annealing twins (Fig. 3d) – they are considerably wider when compared to the narrow deformation twins (Fig. 3e,f).

Fig. 4a presents the density of HAGBs (ρ_{HAGB}) in meters of HAGBs (including twin grain boundaries) per meter-cube of material as a function of the amount of applied cold-rolling. The grain boundary length was obtained by conducting grain boundary analysis on multiple EBSD orientation maps using the MTEX toolbox in MATLAB [25]. It is evident from Fig. 4a that ρ_{HAGB} per unit volume of material has increased by an order of magnitude from the as-received (annealed) condition to the 30% cold-rolled condition. The grain boundary analysis shown in Fig. 3 (bottom) indicates that the observed increase in ρ_{HAGB} can be attributed to the formation of deformation twins as well as new HAGBs that form as a result of the accumulation and rearrangement of dislocations.

The density of geometrically-necessary dislocations[1] (ρ_{GND}) was estimated from EBSD orientation maps by using the mathematical framework proposed by Pantleon [31], employing the MTEX toolbox [25]. Fig. 4b presents the individual EBSD measurements of ρ_{GND} (small full symbols) as well as microstructure-average (bulk) ρ_{GND} (large open symbol) as a function of the amount of applied cold-rolling. As expected based on Ashby's formulation [32], ρ_{GND} increases linearly with applied strain (i.e. amount of cold-rolling). The continuous storage of GNDs is necessary in order to accommodate for the increased deformation gradients that cause lattice curvature (rotation). By doing so, the compatible deformation of polycrystalline aggregates is maintained [33, 34]. With increasing amounts of applied deformation (cold-rolling), present GNDs arrange themselves into low-energy dislocation structures (LEDSs) [35] thus giving rise to both high-angle grain boundaries (HAGBs), and low-angle grain boundaries (LAGBs) that divide grains into sub-grains. With an increasing amount of applied deformation during cold-rolling, the amount of GNDs accumulated at LAGBs increases and so too does the lattice curvature (misorientation), leading to the formation of grain boundaries that are then classified as HAGBs.

In order to obtain the total dislocation density (ρ_T) and the average size of coherently scattering domains ($\langle X \rangle_a$), peak profile (broadening) analysis of the full HRND patterns (see Appendix 1) was performed using the CMWP software packages [26-28]. Note, that ρ_T refers to the overall amount of dislocations - the cumulative sum of both geometrically-necessary dislocations (GNDs), and statistically-stored dislocations[2] (SSDs). The results of peak profile analysis are shown in Fig. 5 – where Fig. 5a presents ρ_T, ρ_{GND} , ρ_{HAGB} (note logarithmic scale) and Fig. 5b presents $\langle X \rangle_a$ as a function of the amount of cold-rolling applied. Note, that the $\langle X \rangle_a$ is related to the CSDs (sub-grain) size. The EBSD and HRND measurements are summarized in Table 3.

It is clear from Fig. 5a and Table 3 that the HRND-measured ρ_T is significantly higher than the EBSD-measured ρ_{GND}. This suggests that both GNDs and SSDs contribute to the work-

[1] Geometrically-necessary dislocations (GNDs) have non-zero Burger's vector, hence they give rise to the lattice curvature detected by EBSD measurements. GNDs are stored in the material in order to maintain strain compatibility across the microstructure, and are therefore referred to as *necessary*.

[2] Statistically-stored dislocations (SSDs) have a net-zero Burgers vector at the microscopic length scale and thus have no geometrical consequence – they do not cause the lattice curvature at this length scale, and are thus not detected by EBSD measurement. SSDs are stored in material via statistical (random) mutual trapping.

hardening of the material and lead to the increased strength and hardness of the alloy in the cold-rolled condition (see Table 2). It is, however, interesting to note that unlike ρ_{GND}, ρ_T does not increase linearly with the amount of applied cold-rolling (strain) but rather plateaus out (saturates at about 2.5E15 m/m^3). This shows that the material cannot store ever-increasing amounts of SSDs, and that dislocation annihilation is taking place during the cold-rolling process [36]. As noted by Ashby [32], the amount of stored SSDs is a characteristic of the material and will thus not keep increasing with increasing strain. The amount of stored SSDs is also unaffected by the grain size or other microstructural characteristics, unlike the amount of stored GNDs.

The peak profile analysis of full diffraction patterns using CMWP also allows to obtain information on the dislocation character (M), see Table 3. A large value of M indicates no dipole character and a value of around 1-3 is indicative of strong dipole character of present dislocations. As contended by Kuhlmann-Wilsdorf [35], with increasing strain, energetically favourable dipolar structures form, which break original grains into CSDs (sub-grains) containing a fewer spread of lattice orientations. Accumulation and arrangements of GNDs into LEDSs leads to formation of HAGBs and LAGBs. However, it needs to be noted that within LEDSs, the edge dislocations of opposite sign can interact and disintegrate leading to their annihilation [35]. Additionally, the observed decreasing size of the coherently scattering domains ($\langle X \rangle_a$) with increasing amount of applied cold-rolling shown in Fig. 5b can be also directly attributed to rearrangements of GNDs into LEDSs [35, 37, 38].

3.2 Effect of cold-rolling on molten salt corrosion

The negative effect of cold-rolling on the molten-salt corrosion resistance of the alloy is immediately apparent from Fig. 6, which plots the recorded mass loss of the studied alloy conditions during exposure to FLiNaK molten salt at 600 °C after 300 hours. It is clear from Fig. 6, that the mass loss is approximately linearly proportional to the amount of applied cold-rolling, wherein the mass loss increases with increased amount of imparted plastic strain (cold-rolling). The SEM micrographs shown in Fig. 7 compliment the results in Fig. 6 and highlight the extent of molten salt corrosion attack on the microstructure. It is clear from Fig. 7 that the most prominent features undergoing enhanced corrosion penetrating into the material are the δ-ferrite regions and grain boundaries of the γ-austenite matrix. Note, that the volume fraction of the δ-ferrite is the same in all sample conditions (about 5 wt.%). It can further be seen from Fig. 7 that the γ-austenite matrix in annealed (0%) specimen is the least affected by exposure to FLiNaK molten salt. Note, that the original sample surface (polished) is still present in the 0% specimen, whilst it is fully corroded away in the 30% specimen. It can be thus concluded that the cold-rolled specimens (20%, 30%) exhibit significantly pronounced corrosion attack of γ-austenite via intergranular corrosion in addition to corrosion attack on the δ-ferrite, which remains similar at all levels of cold-rolling. Table 4 summarises the corrosion results, i.e. the mass loss, and average corrosion penetration depths in both γ-austenite and δ-ferrite.

It can be seen in Fig. 7 and from the corrosion depth measurements in Table 4 that regardless of the amount of cold rolling, the present δ-ferrite stringers undergo consistently higher corrosion attack than the surrounding γ-austenite matrix. The results in Table 4 also highlight the fact that the depth of corrosion of δ-ferrite remains roughly constant irrespective of amount of applied cold-rolling. To understand the reasons for enhanced corrosion of δ-ferrite, Energy-Dispersive Spectroscopy (EDS) maps of the annealed (0%) specimen were obtained and are shown in Fig. 8. It is clear that δ-ferrite is rich in Cr, which is known to readily undergo fluoridation [5]. This is due to the lower Gibbs Free Energy of formation of Cr-rich fluorides (CrF_3 and CrF_4) and higher stability of corrosion products when compared to other metallic fluorides i.e. FeF_2 and MoF_3. Thus, the Cr-rich δ-ferrite will undergo accelerated corrosion when compared to γ-austenite matrix. In addition, the EDS maps in Fig. 8 highlight the presence of brittle Mo-rich σ-phase intermetallics within the δ-ferrite stingers. The formation of σ-phase can be attributed to the decomposition of the δ-ferrite at high temperatures i.e. during the solution annealing (1038^{o}C). These brittle fragments could act as sites of premature cracking and enhance phenomena such as stress corrosion cracking (SCC). However, due to the low volume fraction of σ-phase (<< 1%) in the studied alloy, its effect on the overall corrosion resistance is assumed to be negligible.

In order to identify the leaking of alloying elements from the alloy samples during corrosion, elemental analysis of the salt and microstructure post- corrosion was performed employing Inductively-Coupled-Plasma Mass Spectrometer (ICP-MS), and Electron Probe Micro-Analyzer (EPMA), respectively. ICP-MS results shown in Table. 5 reveal the leaking of Fe, Cr, Mo, Ni, and Mn into the molten salt. It is further clear that no chemical equilibrium (saturation) was reached in any element concentration between the alloy (Table 1) and molten salt (200 g) during the test (300 h). EPMA results in Fig. 9 highlight the diffusion of alloying elements towards the grain boundaries and the formation of metallic fluorides (corrosion products) and carbides (sensitisation). It is important to note that whilst diffusion of alloying elements and the formation of corrosion products at grain boundaries will occur in all of the samples (0%, 20% and 30% cold-rolled), samples with higher levels of cold rolling will be more affected. This is due to the increased prevalence of high diffusion pathways (i.e. grain boundaries, dislocations - see Figs. 4 and 5) wherein alloying elements can readily interact with the salt constituents in order to form more stable fluorine-based corrosion products or carbides. In particular, it was shown by Zhou et al.,[39] that Cr will more readily diffuse to HAGBs rather than LABGs and thus with increased levels of cold rolling, there will be increased Cr diffusion at these regions and hence enhanced corrosion. Furthermore, Zheng et al's. [17] observations of the 316L alloy in FLiBe at 700^o for 3000h showed the formation of $MoSi_2$ agglomerates at the grain boundaries.

The extent of formation of Cr-rich (CrF_3, CrF_4) and Mo-rich (MoF_3) corrosion products at the grain boundaries can be attributed to the high redox potential of the molten salt due to the presence of impurities. Appendix 1 highlights that there is a significant amount of SO_4^{2-} (≤240 ppm) initially present within the molten salt mixture. It has been shown in Ref. [40] that the presence of SO_4^{2-} within the salt encouraged the oxidation of Cr into Cr_2O_3, and it also promotes

the formation of polyvalent metallic Mo ions [41]. Leaking of Mo is further prompted by the presence of H_2O (moisture) and O in the salt - studies conducted by Ouyang et al. [6], highlight that increased moisture enhances the depletion of the Mo. Similarly to SO_4^{2-}, the presence of Cl^- reduces the corrosion resistance of Ni and Fe alloys due to the leaching of Cr and Fe and the formation of pits within the microstructure [42]. The FLiNaK salt utilised in the current experiment contains ≤ 65ppm of Cl^- which could promote the depletion of both of these elements. This is because when exposed to Cl^-, both Fe and Cr oxides readily react in order to produce $CrCl_3$ as well as $FeCl_2$ [43]. Thus, the presence of Cl^- at high temperatures can explain the significant depletion of Fe as it is able to penetrate through the destabilised Cr_2O_3 layer and attack the Fe. It is evident, that even small amounts of impurities within the salt can have a significant role on the corrosion performance of structural alloys. It is important to note however, that in here present experiment all the tested samples were exposed to salt of the same chemical composition and duration in one single corrosion test. Thus, although the presence of impurities is an important consideration for operation of future MSR and CST-TES energy-generation and energy-storage systems, for the purpose of this study, the effect of present impurities is not specifically considered as it is the same for all studied samples.

In order to evaluate the effect of cold-rolling on molten salt corrosion, the obtained microstructure characteristics - density of HAGBs (ρ_{HAGB}), GNDs (ρ_{GNDs}), total dislocation density (ρ_T) in the unit volume of material [m/m^3] and the average size of coherently scattering domains ($\langle X \rangle_a$) as a function of recorded mass loss are shown in Figs. 10 and 11, respectively. It becomes apparent from present results that the material mass loss, which reflects the corrosion rate and thus extent of corrosion attack, is strongly dependant on these microstructural characteristics. This is particularly highlighted in Fig. 10a where it is clear that the alloy mass loss during the exposure to the molten salt is directly proportional to the increased prevalence of both GNDs and HAGBs. It is believed that the lower atom coordination (broken periodicity of crystal lattice) at HAGBs and GNDs leads to the higher diffusivity of alloying elements and higher salt penetration into the sample, resulting in accelerated corrosion of the alloy in the cold-rolled condition.

A high tendency for Cr to undergo sensitization at temperatures of 500-800°C and migrate to regions such as HAGBs and GNDs [44] further reduces the amount of Cr in solid-solution in addition to the above-described formation of Cr fluorides. The EPMA results highlight the prevalence Cr carbide precipitates along the grain boundaries (Fig. 9d,e) affirming that sensitization is taking place during exposure to the molten salt. This in turn generates a localised electrochemical cell, wherein the Cr depleted regions surrounding the sensitized region become the anode leading to galvanic corrosion and thus fluoridation of Fe [45] and its leaking to the molten salt as confirmed by ICP-MS analysis (Table 5). Interestingly, ICP-MS analysis revealed that there is a lower amount of Cr present within the salt when compared to Fe, although the Gibbs free energy of formation of Cr rich fluorides is lower. This could be attributed to significantly higher content of Fe in the alloy, and possibly to the interaction between the alloy and the carbon crucible where, as contended by Olson et al. [46], Cr

dealloying can occur through a process known as nonelectric transfer (see Refs [46-48]). This process is particularly prominent in FLiNaK salt because of its capability to form Cr rich fluorides of different valence states [5]. At high temperatures, Cr fluorides with low oxidation states present in the molten salt undergo a reaction with the carbon crucible and form Cr carbides, which might deposit on the surface of the crucible. Thus, the Cr from the molten salt is effectively being removed from molten salt during the corrosion test, which could explain the lower amounts of Cr detected within the salt, post-corrosion testing.

Moreover, as the extent of cold rolling increases, more HAGBs and GNDs are generated, which will promote sensitization process and thus promote corrosion of the alloy via galvanic corrosion. The above is also true for SSDs, however, because SSDs have zero Burger's vectors [32], their presence does not cause significant atomic mis-arrangements of the crystal lattice when compared to HAGBs and GNDs. This is highlighted in Figs.10a,10b,11a when comparing the EBSD-measured ρ_{HAGB}, ρ_{GNDs} and HRND-measured ρ_T results as a function of material mass loss during the corrosion testing - there is a more pronounced relationship between mass loss and ρ_{HAGB}, ρ_{GNDs} rather than ρ_T. This is particularly clear when comparing the 20 and 30% conditions – note that despite hardly small change in the stored total dislocation density (ρ_T) significant mass loss is recorded. Hence, the mass loss (corrosion) is primarily governed by the presence of HAGBs and GNDs – the higher the amount of HAGBs and GNDs the higher the corrosion rate.

Furthermore, Hartley [49] contends that, due to the established interaction energy gradient that exists between alloying elements and dislocations, alloying elements preferentially migrate along the dislocations towards the grain boundaries. In addition, Hartley argues that solute atoms will preferentially migrate to existing dipole structures - the prevalence of which has been shown to increase with increased amount of cold-rolling (see M factor in Table 3, and discussion in section 3.1). The effect of all of the above phenomena is that the chemical composition of these regions (HAGBs, Dislocation Structures) is different to the bulk material as shown by the EPMA maps - Fig. 9. It is apparent that the bulk material has a uniform distribution of both Fe and Ni, whilst Cr-rich corrosion products are concentrated at the grain boundaries (including twin boundaries). It is important to note that whilst a significant increase in dipole characteristics is observed with increased amount of cold-rolling, the effects of solute-dipole drift will be much weaker than those observed at grain boundaries but could still lead to some extent of electrochemical corrosion and hence increased mass loss within the structure. In addition, Fig.11b shows that with increased sub-grain (CSDs) formation, the mass loss increases due to the prevalence of LEDSs enclosing coherently diffracting regions. This further results in increased grain boundary length and density of dislocation structures leading to exacerbated corrosion by the aforementioned mechanisms.

Finally, it is believed that atoms located at the HAGBs, LAGBs and GNDs are more active than bulk atoms and are hence more energetically likely to undergo fluoridation. Ahmadkhaniha et al. [50] highlighted that the presence of grain boundaries leads to higher

rates of diffusion and lower atom coordination (i.e. a decreased surface work function) resulting in increased rates of removal of material at these boundaries i.e. by fluoridation. In addition, the significant increase in grain boundary length in cold-rolled samples is partly caused by profuse deformation twinning (see Fig. 3). It can thus be concluded that both dislocation slip, and deformation twinning leads to worsening of corrosion resistance (enhanced mass loss) of the 316L alloy by introduction of new grain boundaries (HAGBs). Similarly, Aung et al. [51] found that the prevalence of twins in Mg alloy (AZ31B) increased the extent of intragranular corrosion within a 3.5% NaCl solution. The EPMA result in Fig. 9 affirm this theory as they highlight the depletion of Fe and Ni and enrichment of Cr rich corrosion products at the twin regions (labelled in Fig.9a).

4. Conclusion

In order to evaluate the effect of the cold-rolling on the corrosion resistance of the 316L alloy at three different levels of cold rolling (0%, 20% and 30%), the samples were immersed in molten FLiNaK at 600^{o}C for 300h. It is evident from the present results that cold rolling process increases the susceptibility of 316L alloy to corrosion attack in FLiNaK molten salt. This is manifested by increased material mass loss and measured corrosion depths. It is shown that the recorded material mass loss, which is related the extent of corrosion attack is primarily governed by the presence of HAGBs and GNDs and to a lesser extent to the presence of SSDs – the higher amount of stored HAGBs and GNDs leads to a greater extent of corrosion attack. This is due to the enhanced diffusion of alloying elements in particular Cr, Mo to HAGBs and GNDs where they can readily react with compounds of FLiNaK salt leading to formation of corrosion products (fluorides), which then dissolve into the molten salt. It is further shown that the corrosion attack of δ-ferrite remains approximately constant irrespective of the amount of applied cold-rolling. This suggests that the corrosion of the γ-austenite (matrix) is governed by microstructural characteristics (i.e. presence of HAGBs, GNDs, SSDs), while corrosion of the Cr-rich δ-ferrite is governed by low Gibbs Free Energy of formation of Cr-rich fluorides.

Acknowledgment

The authors would like to thank Mr Paul Crooker from Electric Power Research Institute (EPRI) for the support of the project and American Stainless Steel Corporation for providing the 316L alloy. The authors thank Dr Karen Privat for technical assistance and use of facilities supported by AMMRF at the Electron Microscope Unit at UNSW. The authors would like to further acknowledge Mr Jordan Keirle for his contribution to the project during his Honours project at ANSTO and UNSW. This research is supported by the AINSE Honours Scholarship Program.

References:

1. Serp, J., et al., *The molten salt reactor (MSR) in generation IV: Overview and perspectives.* Progress in Nuclear Energy, 2014. **77**(Supplement C): p. 308-319.
2. Elsheikh, B.M., *Safety assessment of molten salt reactors in comparison with light water reactors.* Journal of Radiation Research and Applied Sciences, 2013. **6**(2): p. 63-70.

3. Moir, R.W. and E. Teller, *Thorium-Fueled Underground Power Plant Based on Molten Salt Technology*. Nuclear Technology, 2005. **151**(3): p. 334-340.
4. Zhao, Z., M.T. Arif, and M.T.O. Amanullah, *Solar Thermal Energy with Molten-salt Storage for Residential Heating Application*. Energy Procedia, 2017. **110**(Supplement C): p. 243-249.
5. Olson, L.C., et al., *Materials corrosion in molten LiF–NaF–KF salt*. Journal of Fluorine Chemistry, 2009. **130**(1): p. 67-73.
6. Ouyang, F.-Y., et al., *Effect of moisture on corrosion of Ni-based alloys in molten alkali fluoride FLiNaK salt environments*. Journal of Nuclear Materials, 2013. **437**(1): p. 201-207.
7. Sawant, S.S., et al., *High Temperature Corrosion Studies in Molten Salt Using Salt Purification and Alloy Coating*. Indian Chemical Engineer, 2017. **59**(3): p. 242-257.
8. Sona, C.S., et al., *High temperature corrosion studies in molten salt-FLiNaK*. Corrosion Engineering, Science and Technology, 2014. **49**(4): p. 287-295.
9. Allen, T., et al., *Materials challenges for nuclear systems*. Materials Today, 2010. **13**(12): p. 14-23.
10. Zinkle, S.J. and J.T. Busby, *Structural materials for fission & fusion energy*. Materials Today, 2009. **12**(11): p. 12-19.
11. Marquis, E.A., et al., *Nuclear reactor materials at the atomic scale*. Materials Today, 2009. **12**(11): p. 30-37.
12. Yvon, P. and F. Carré, *Structural materials challenges for advanced reactor systems*. Journal of Nuclear Materials, 2009. **385**(2): p. 217-222.
13. Sellers, R.S., et al., *Corrosion of 316L Stainless Steel Alloy and Hastelloy-N Superalloy in Molten Eutectic LiF-NaF-KF Salt and Interaction with Graphite*. Nuclear Technology, 2014. **188**(2): p. 192-199.
14. Zhong, Y., et al., *Additive manufacturing of 316L stainless steel by electron beam melting for nuclear fusion applications*. Journal of Nuclear Materials, 2017. **486**(Supplement C): p. 234-245.
15. Cattant, F., D. Crusset, and D. Féron, *Corrosion issues in nuclear industry today*. Materials Today, 2008. **11**(10): p. 32-37.
16. Ishiyama, N., et al., *Stress Corrosion Cracking of Type 316 and 316L Stainless Steel in High Temperature Water*. 2005.
17. Zheng, G., et al., *Corrosion of 316 stainless steel in high temperature molten Li2BeF4 (FLiBe) salt*. Journal of Nuclear Materials, 2015. **461**(Supplement C): p. 143-150.
18. Desu, R.K., et al., *Mechanical properties of Austenitic Stainless Steel 304L and 316L at elevated temperatures*. Journal of Materials Research and Technology, 2016. **5**(1): p. 13-20.
19. Milad, M., et al., *The effect of cold work on structure and properties of AISI 304 stainless steel*. Journal of Materials Processing Technology, 2008. **203**(1): p. 80-85.
20. Ilevbare, G., et al., *Program on Technology Innovation: Proceedings : 2007 AECL/COG/EPRI Workshop on Cold Work in Iron- and Nickel-Base Alloys Exposed to High Temperature Water Environments : June 3-8, 2007, Mississauga, Ontario*. 2008: Electric Power Research Institute.
21. Andresen, P.L. and C.L. Briant, *Environmentally Assisted Cracking of Types 304L/316L/316NG Stainless Steel in 288°C Water*. CORROSION, 1989. **45**(6): p. 448-463.
22. Toby, B.H. and R.B. Von Dreele, *GSAS-II: the genesis of a modern open-source all purpose crystallography software package*. Journal of Applied Crystallography, 2013. **46**(2): p. 544-549.
23. Bachmann, F., R. Hielscher, and H. Schaeben, *Texture Analysis with MTEX – Free and Open Source Software Toolbox*. Solid State Phenomena, 2010. **160**: p. 63-68.
24. Reiche, H. and S. Vogel, *A versatile automated sample changer for texture measurements on the high pressure-preferred orientation neutron diffractometer*. Review of Scientific Instruments, 2010. **81**(9): p. 093302.

25. MathWorks, I., *MATLAB : the language of technical computing : computation, visualization, programming : installation guide for UNIX version 5*. 1996: Natwick : Math Works Inc., 1996.
26. Ungar, T., et al., *The contrast factors of dislocations in cubic crystals: the dislocation model of strain anisotropy in practice.* Journal of Applied Crystallography, 1999. **32**(5): p. 992-1002.
27. Ribárik, G. and T. Ungár, *Characterization of the microstructure in random and textured polycrystals and single crystals by diffraction line profile analysis.* Materials Science and Engineering: A, 2010. **528**(1): p. 112-121.
28. G. Ribárik, B.J.a.T.U., *Monte-Carlo and least-squares procedures combined for global minimum of the physical parameters in line profile analysis. in preparation.*
29. Balogh, L., G. Ribárik, and T. Ungár, *Stacking faults and twin boundaries in fcc crystals determined by x-ray diffraction profile analysis.* Journal of Applied Physics, 2006. **100**(2): p. 023512.
30. Balogh, L., G. Tichy, and T. Ungar, *Twinning on pyramidal planes in hexagonal close packed crystals determined along with other defects by X-ray line profile analysis.* Journal of Applied Crystallography, 2009. **42**(4): p. 580-591.
31. Pantleon, W., *Resolving the geometrically necessary dislocation content by conventional electron backscattering diffraction.* Scripta Materialia, 2008. **58**(11): p. 994-997.
32. Ashby, M.F., *The deformation of plastically non-homogeneous materials.* The Philosophical Magazine: A Journal of Theoretical Experimental and Applied Physics, 1970. **21**(170): p. 399-424.
33. Arsenlis, A. and D.M. Parks, *Crystallographic aspects of geometrically-necessary and statistically-stored dislocation density.* Acta Materialia, 1999. **47**(5): p. 1597-1611.
34. Fleck, N.A., M.F. Ashby, and J.W. Hutchinson, *The role of geometrically necessary dislocations in giving material strengthening*. Scripta Materialia, 2003. **48**(2): p. 179-183.
35. Kuhlmann-Wilsdorf, D., *LEDS: Properties and effects of low energy dislocation structures.* Materials Science and Engineering, 1987. **86**: p. 53-66.
36. Ungár, T., et al., *Work softening in nanocrystalline materials induced by dislocation annihilation.* Scripta Materialia, 2011. **64**(9): p. 876-879.
37. Kuhlmann-Wilsdorf, D. and N. Hansen, *Geometrically necessary, incidental and subgrain boundaries*. Scripta Metallurgica et Materialia, 1991. **25**(7): p. 1557-1562.
38. Hughes, D., N. Hansen, and D. Bammann, *Geometrically necessary boundaries, incidental dislocation boundaries and geometrically necessary dislocations*. Scripta Materialia, 2003. **48**(2): p. 147-153.
39. Zhou, X., et al., *Grain Boundary Specific Segregation in Nanocrystalline Fe(Cr) OPEN*. Vol. 6. 2016. 34642.
40. Zhu, Y., et al., *Effects of SO42− ions on the corrosion of GH3535 weld joint in FLiNaK molten salt.* Journal of Nuclear Materials, 2017. **492**: p. 122-127.
41. Kondo, M., *High performance corrosion resistance of nickel-based alloys in molten salt flibe.* Fusion Science and Technology, 2009. **56**(1): p. 190-194.
42. Saboktakin, M., et al., *Effect of Chlorine Ion on the Corrosion of 316L Austenitic Stainless Steel*. Vol. 23. 2017. 1-12.
43. Porcayo-Calderón, J., et al., *Electrochemical Study of Ni20Cr Coatings Applied by HVOF Process in ZnCl(2)-KCl at High Temperatures.* Journal of Analytical Methods in Chemistry, 2014. **2014**: p. 503618.
44. Laws, M.S. and P.J. Goodhew, *Grain boundary structure and chromium segregation in a 316 stainless steel.* Acta Metallurgica et Materialia, 1991. **39**(7): p. 1525-1533.
45. Kondo, M., et al., *Metallurgical study on corrosion of austenitic steels in molten salt LiF–BeF2 (Flibe)*. Journal of Nuclear Materials, 2009. **386-388**: p. 685-688.

46. Olson, L.C., et al., *Impact of Corrosion Test Container Material in Molten Fluorides*. Journal of Solar Energy Engineering, 2015. **137**(6): p. 061007-061007-8.
47. Ozeryanaya, I.N., *Corrosion of metals by molten salts in heat-treatment processes*. Metal Science and Heat Treatment, 1985. **27**(3): p. 184-188.
48. S. Sellers, R., et al., *Corrosion of 316L stainless steel alloy and Hastelloy-N superalloy in molten eutectic LiF-NaF-KF salt and interaction with graphite*. Vol. 188. 2014. 192-199.
49. Hartley, C., *Kinetics of solute atom drift to dislocation dipoles*. Acta Metallurgica, 1970. **18**(2): p. 271-273.
50. Ahmadkhaniha, D., et al., *Corrosion behavior of severely plastic deformed magnesium based alloys: A review*. Surface Engineering and Applied Electrochemistry, 2017. **53**(5): p. 439-448.
51. Aung, N.N. and W. Zhou, *Effect of grain size and twins on corrosion behaviour of AZ31B magnesium alloy*. Corrosion Science, 2010. **52**(2): p. 589-594.

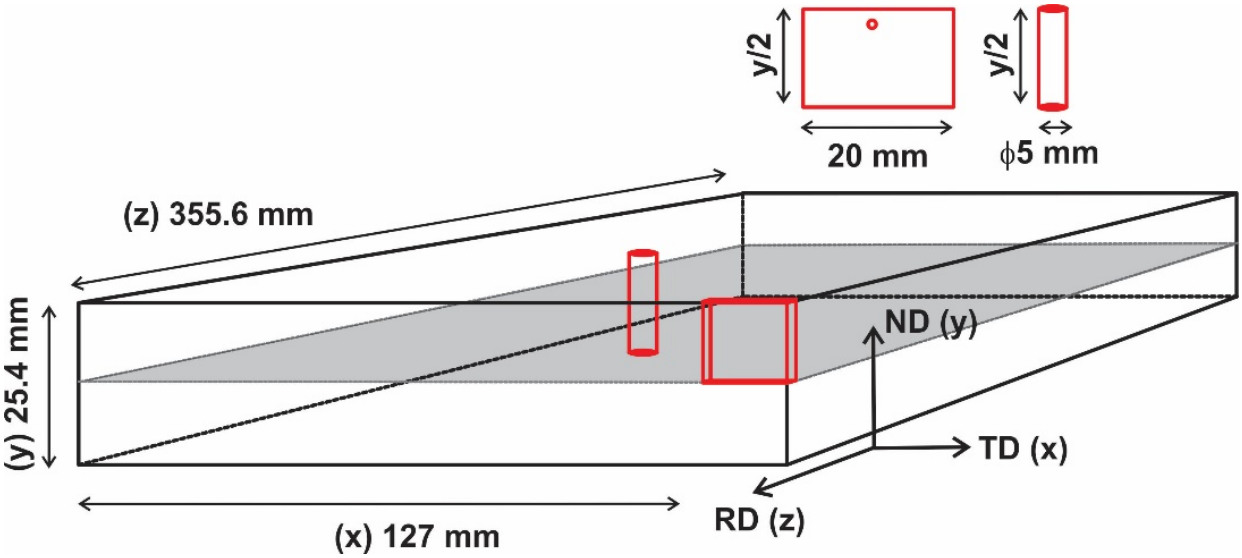

Fig. 1: A schematic representation of received AISI 316L (610344-3A) plate before cold-rolling and EDM extraction of samples for molten salt testing and neutron diffraction measurements. (a) The samples extracted for corrosion testing with dimensions 20 × y/2 × 2 mm, where y is the thickness of the plate after 0%, 20% and 30% reduction in thickness by cold rolling. (b) The extracted cylindrical samples for neutron diffraction measurements with a 5 mm in diameter and y/2 height.

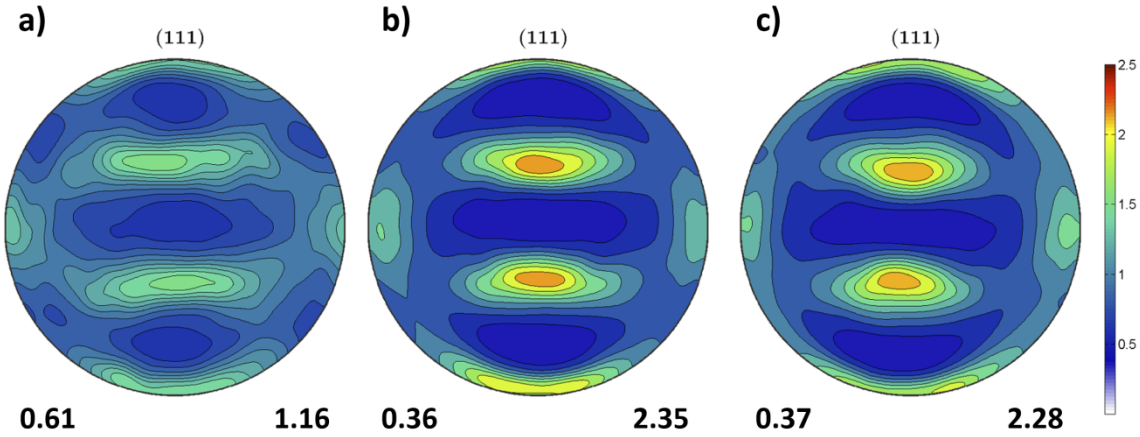

Fig. 2: The texture measurements of studied 316L alloy – recalculated 111 pole figure: (a) 0%, (b) 20% and (c) 30% of cold-rolling. The measurements were collected using High-Intensity Neutron Diffractometer (HIND) ECHIDNA at ANSTO and analysed using MTEX Matlab toolbox.

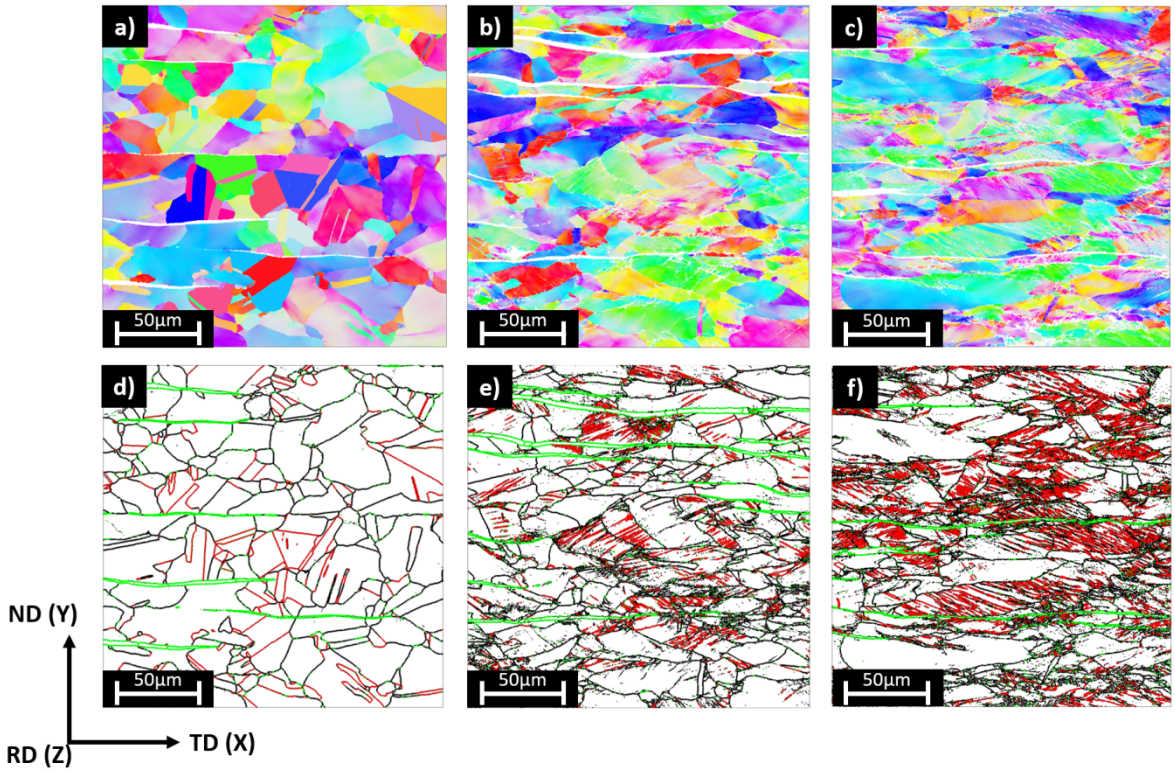

Fig 3: EBSD orientation maps taken at a step size of 0.14 µm: (a,d) 0%, (b,e) 20% and (c,f) 30% cold-rolled 316L alloy conditions. EBSD orientation maps highlight increase in the grain boundary length with increasing amount of imparted cold-rolling deformation - HAGBs (>5° misorientation, black) and twin boundaries (60° misorientation, red). Annealing twins are present in the 0% cold-rolled sample – they are considerably wider comparing to deformation twins.

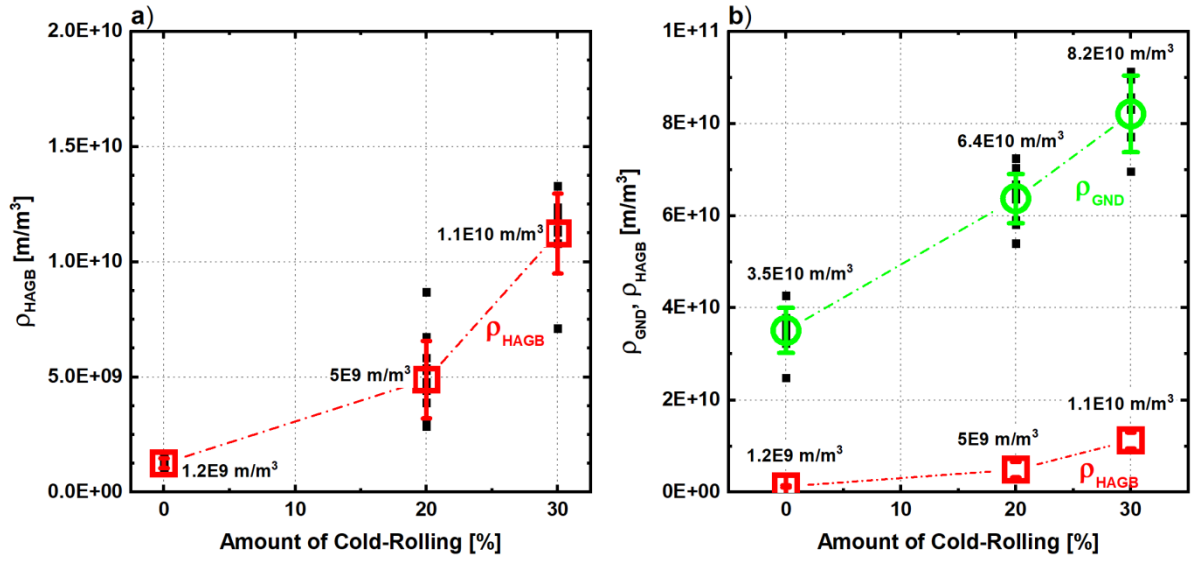

Fig. 4: The EBSD-measured (a) density of High-Angle Grain Boundaries (HAGBs) (ρ_{HAGB}), and (b) Geometrically-Necessary Dislocations (GNDs) (ρ_{GND}) as a function of amount of imparted cold-rolling deformation. Multiple EBSD orientation maps were collected and analysed – see individual measurements (small full symbols) - these were then averaged to obtained microstructure-averaged (bulk) measurements (large open symbols). The analysis of EBSD orientation maps was performed using the MTEX Matlab toolbox.

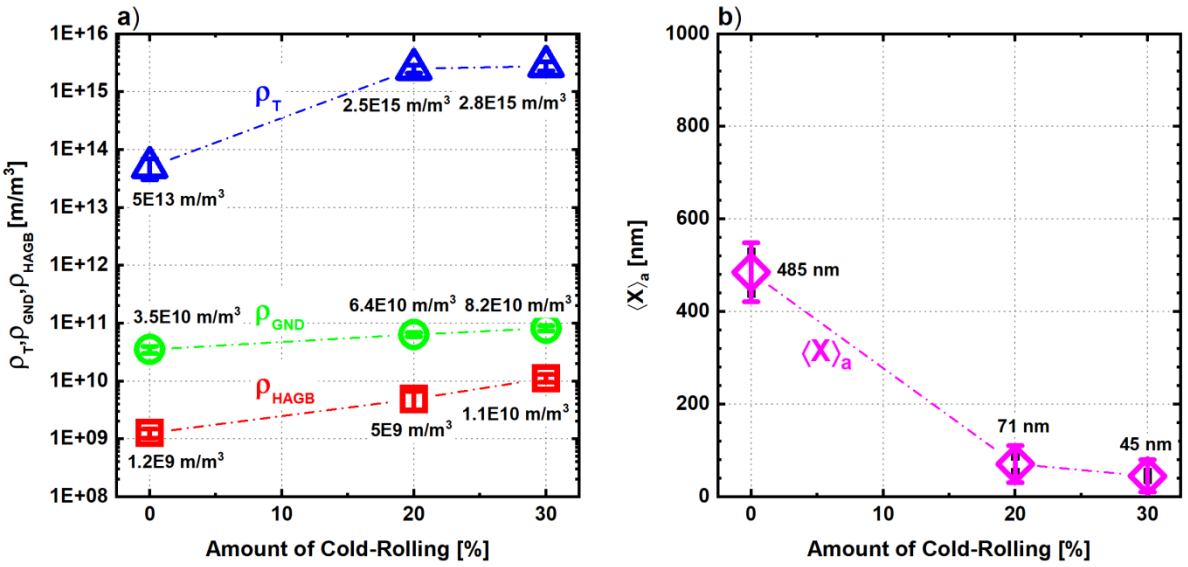

Fig. 5: The HRND-measured (a) total dislocation density (ρ_T) together with ρ_{HAGB}, ρ_{GND} and (b) average size of coherently scattering domains (CSDs) $\langle X \rangle_a$ as a function of amount of imparted cold-rolling deformation. The analysis of HRND patterns was performed using the CMWP software.

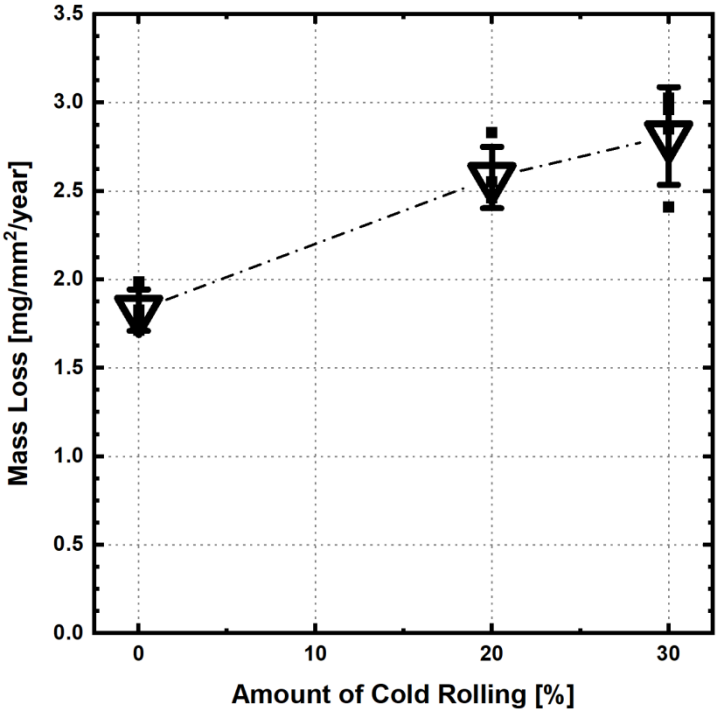

Fig. 6. The recorded material mass loss [mg/mm²/year] of tested 316L alloy conditions (0%,20% and 30%) in FLiNaK at 650°C/300h as a function of amount of imparted cold-rolling deformation.

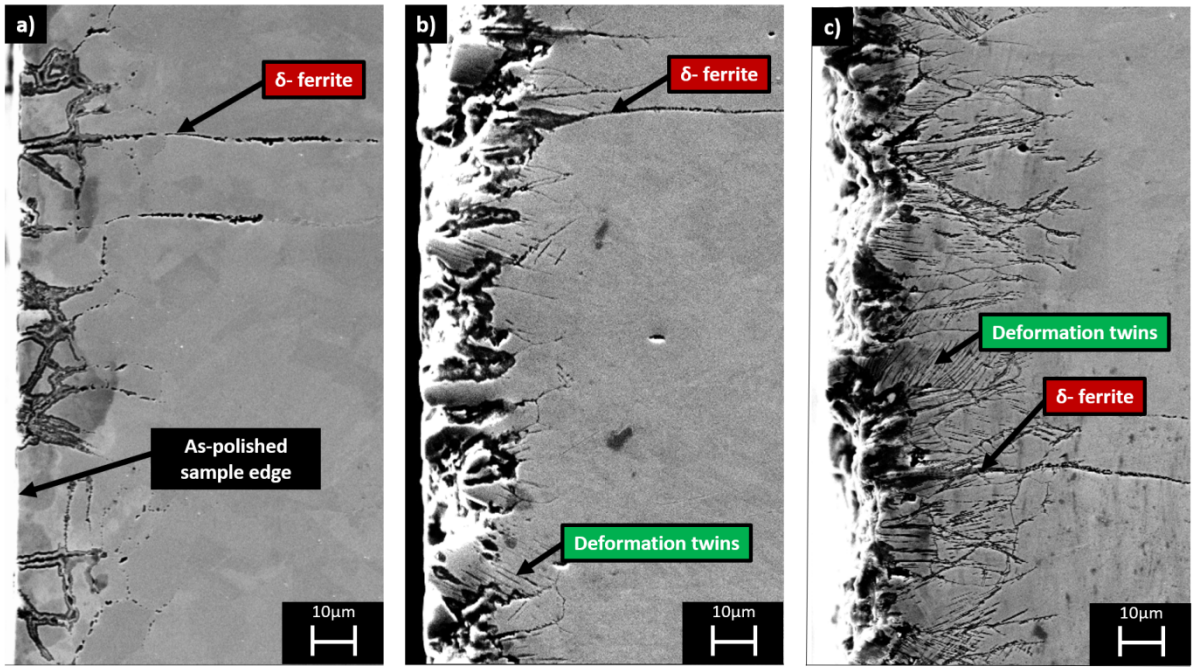

Fig. 7: SEM images of post-corrosion 316L alloy samples at 500x magnification: (a) 0%, (b) 20%, and (c) 30% of amount of imparted cold-rolling deformation.

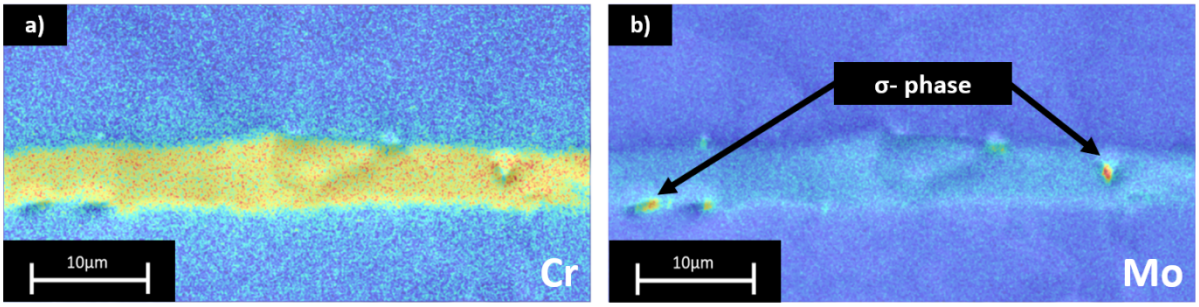

Fig. 8: High-resolution EDS maps of Cr-rich δ-ferrite in as-received alloy – (a) Cr EDS map, (b) Mo EDS map – Mo EDS maps shows the presence of brittle intermetallic σ-phase.

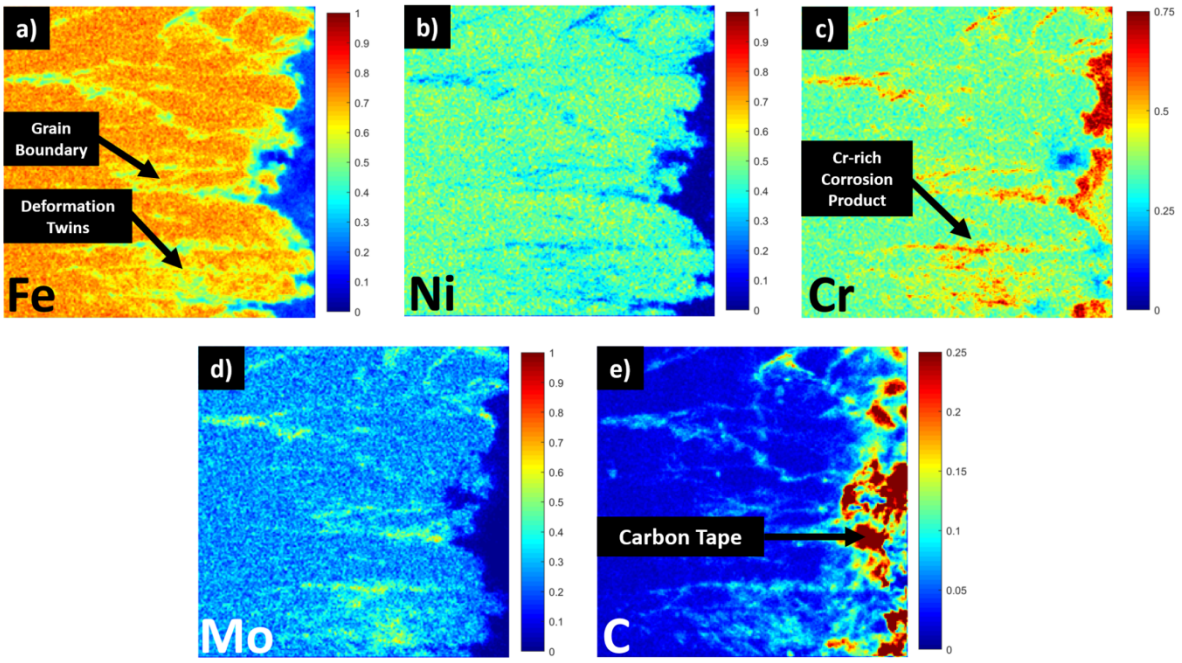

Fig. 9: EPMA maps showing Cr-rich, Mo-rich corrosion products and carbides at the grain boundaries of 30% cold-rolled sample - (a) Fe EPMA map, (b) Ni EPMA map, (c) Cr EPMA map, (d) Mo EPMA map and (e) C EPMA map.

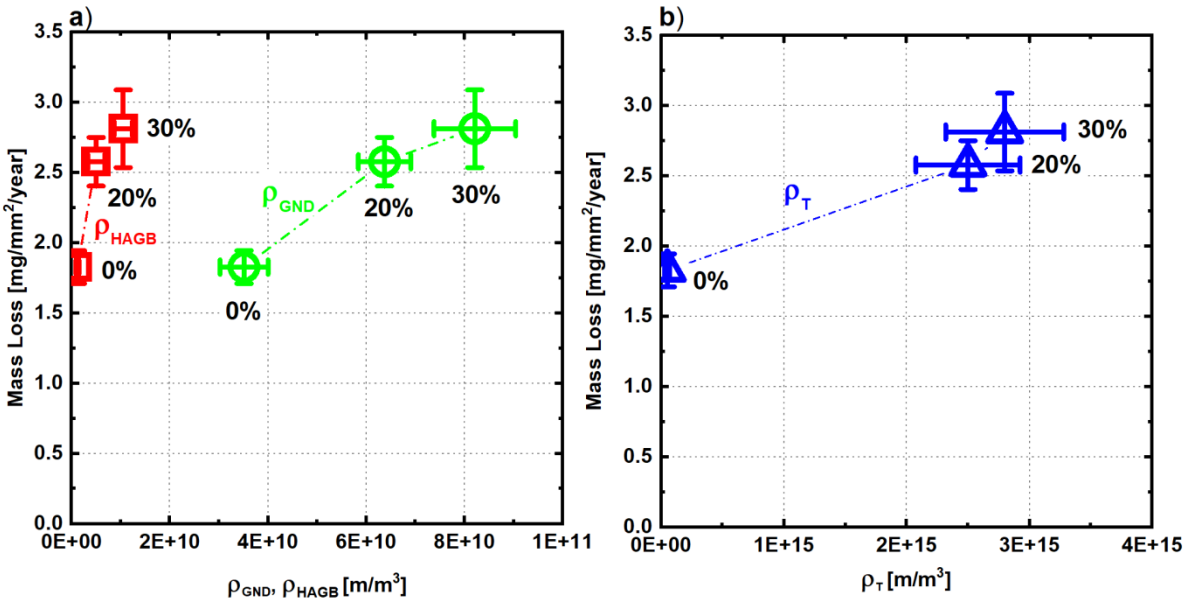

Fig. 10: Material mass loss as a function of (a) EBSD-measured density of HAGBs (ρ_{HAGB}), GNDs (ρ_{GND}) and (b) HRND-measured total dislocation density (ρ_T) for the different levels of cold-rolling conditions (0%, 20% and 30%) of 316L alloy.

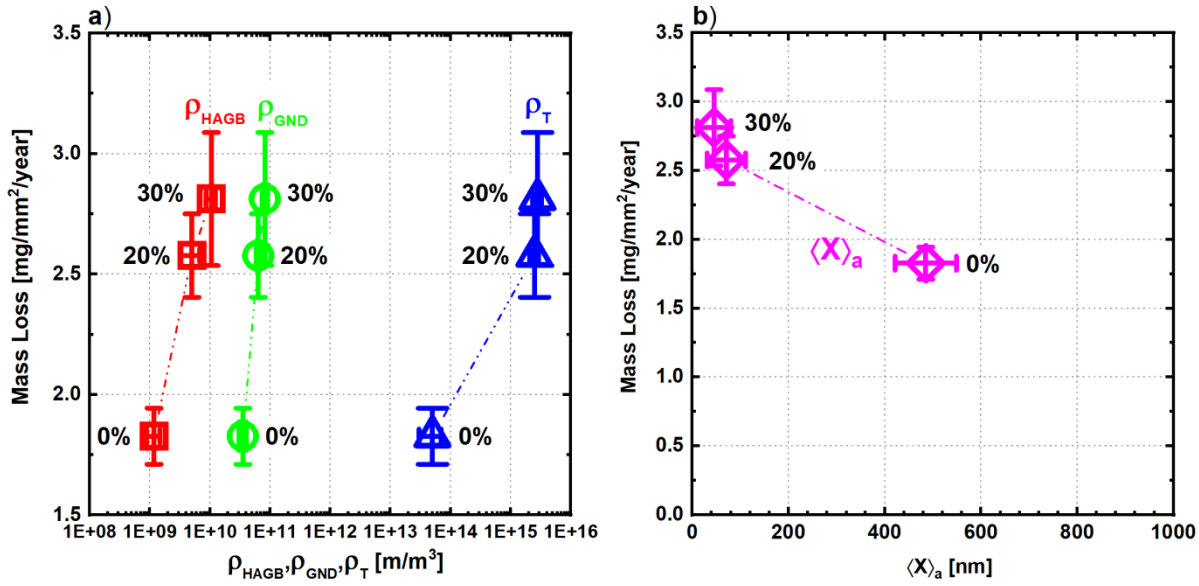

Fig. 11: (a) A summary graph showing the recorded material mass loss as a function of EBSD-measured density of HAGBs (ρ_{HAGB}), GNDs (ρ_{GND}) and HRND-measured total dislocation density (ρ_T) for all tested 316L alloy conditions. (b) The recorded material mass loss as a function of HRND-measured average size of coherently scattering domains (CSDs) $\langle X \rangle_a$.

Appendix 1:

Top figure shows the comparision of HRND patterns of the as-annealed (0%) and 30% cold-rolled samples. The positions of γ-austenite, δ-ferrite and $M_{23}C_6$ (Cr) carbides diffraction peaks are marked by vertical ticks. It becomes apparent from this comparison that diffraction peaks of γ-austenite broadens significanly as a result of imparted plastic strain (cold-rolling). This broadening of diffraction peaks was then evaluated using CMWP software in term of the strain (dislocations) and size of CSDs broadning. Bottom figure shows the HRND experimental data from 30% cold-rolled sample and CMWP model of the this diffraction data. Note that the presence of δ-ferrite and $M_{23}C_6$ diffraction peaks was ignored in the CMWP analysis.

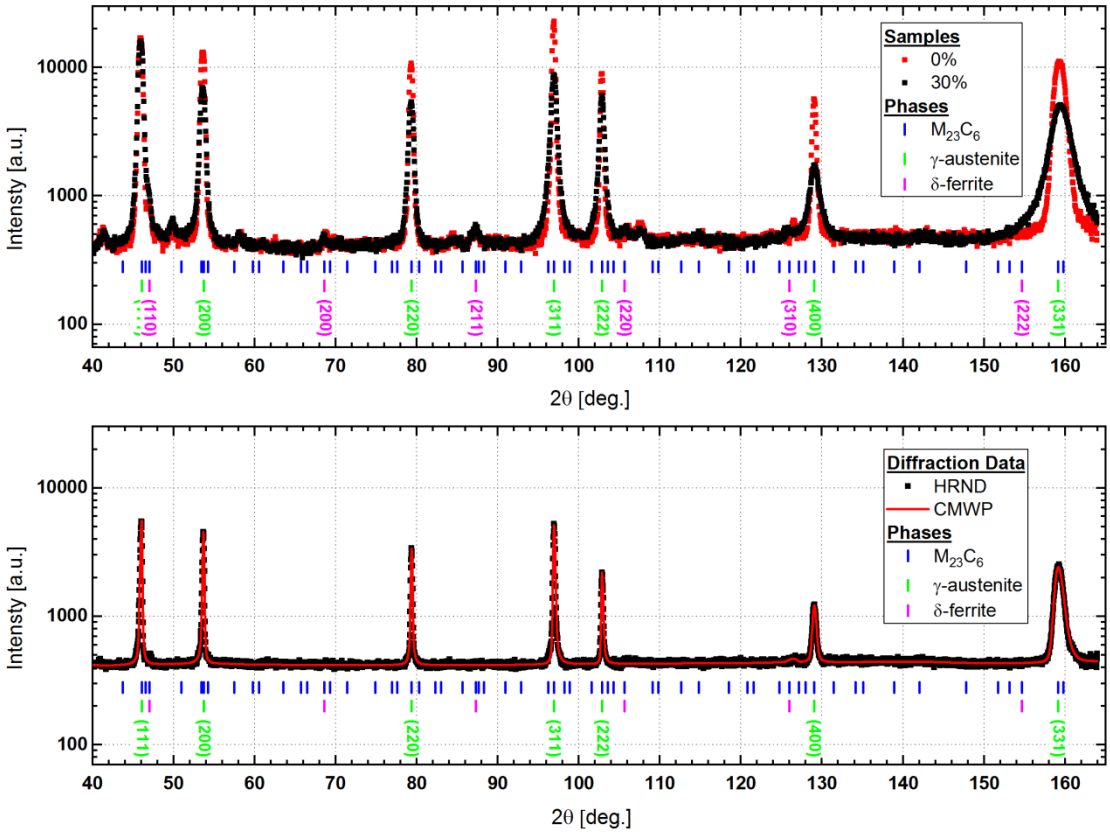

Appendix 2:

The theoretical maximum of impurities present within the used salt from the raw chemical constituents (LiF (62497), NaF (201154) and KF (60239)) supplied by Sigma-Aldrich (≥ 99.0% pure) are shown.

	NaF (ppm)	LiF (ppm)	KF (ppm)	NaF-LiF-KF (FLiNaK) (ppm)
Cl	50	100	50	64.6
S	300	500	100	240
Fe	30	50	5	21.1
Ag	0	0	5	2.95
Al	0	200	5	61.4
As	0	5	0	1.46
Ba	0	50	5	17.6
Bi	0	20	5	8.79
Ca	0	500	10	152
Cd	0	5	5	4.41
Co	0	5	5	4.42
Cr	0	10	5	5.88
Cu	0	50	5	17.56
Fe	30	50	5	21.07
K	200	100	0	52.6
Mg	0	100	5	32.2
Mn	0	5	5	4.42
Mo	0	5	5	4.42
Na	0	500	500	442
Ni	0	100	5	32.2
Pb	30	10	5	9.38
Sr	0	100	5	32.2
Zn	0	10	5	5.88
Li	0	0	5	2.95
Ti	0	0	5	2.95

Table 1. Chemical composition (wt %) of AISI 316L Stainless Steel sourced from the American Stainless Steel Corp.

C	Mn	P	S	Si	Cr	Ni	Co	Cu	Mo	N	Cb	Ti	Al	Sn
0.019	1.59	0.033	0.011	0.35	16.46	10.07	0.32	0.39	2.04	0.03	0.015	0.003	0.003	0.008

Table 2. Final thickness (y) and mechanical properties of the AISI 316L plates including the Yield Strength, Ultimate Tensile Strength, Total Elongation and Rockwell Hardness.

Thickness Reduction [%]	Plate Thickness (y) [mm]	Yield Strength [MPa]	Ultimate Tensile Strength [MPa]	Total Elongation [%]	Rockwell Hardness [-]
0%	25.40	347	602	54	52
20%	20.32	723	863	34	62
30%	17.78	821	957	31	65

Table 3. Summary of EBSD-measured (ρ_{HAGB}, ρ_{GND}) and HRND-measured (ρ_T, $\langle X \rangle_a$ and M) microstructural characteristics, where ρ_{HAGB} is the density of High-Angle Grain Boundaries (HAGBs), ρ_{GND} is the density of Geometrically Necessary Dislocations (GNDs), ρ_T is the total dislocation density, $\langle X \rangle_a$ is the mean size of coherently scattering domains (CSDs), and M is a measure of the dipole character of the dislocations. Note that a high M value indicates no dipole character and a low M value indicates strong dipole character.

	EBSD		HRND		
Amount of Cold Work [%]	ρ_{HAGB} [m/m^3]	ρ_{GND} [m/m^3]	ρ_T [m/m^3]	<x> [nm]	M
0%	1.3E+09 (±2E+08)	3.5E+10 (±5E+09)	5E+13 (± 2E+13)	440 (± 50)	22 (±4)
20%	4.9E+09 (±2E+09)	6.4E+10 (±5E+09)	2.3E+15 (± 2E+14)	53 (± 10)	2.2 (±0.8)
30%	1.1E+10 (±2E+09)	8.2E+10 (±8E+09)	2.1E+15 (±2E+14)	37 (±8)	2.3 (±0.8)

Table 4. Post-corrosion (FLiNaK at 600°C/300h) results highlighting overall recorded material mass loss, and recorded corrosion depths in γ –austenite and δ-ferrite.

Amount of Cold Rolling [%]	Mass Loss [mg/mm^2/year]	ϒ-austenite [µm/year]	δ-ferrite [µm/year]
0	1.8 ± 0.1	996.3 ± 162	3650.3 ± 422
20	2.6 ± 0.2	1172.1 ± 284	3301.6 ± 468
30	2.8 ± 0.3	1686.6 ± 189	3494.9 ± 588

Table 5: ICP-MS analysis of the FLiNaK molten salt before (i.e. after salt-bake out procedure) and after sample testing.

	Fe [ppm]	Cr [ppm]	Mo [ppm]	Ni [ppm]	Mn [ppm]
Before Corrosion Test (i.e. after salt bake out)	0.90	0.090	<0.010	0.088	0.017
After Corrosion Test	6.24	0.334	0.120	0.252	0.115